

SST Pattern Test in ACSPO clear-sky mask for VIIRS

I. Gladkova ^{a,b,c,*}, Y. Kihai ^{a,b}, A. Ignatov ^a, F. Shahriar ^{c,d}, B. Petrenko ^{a,b}

^a NOAA Center for Satellite Applications and Research, United States

^b GST, Inc., United States

^c City College of New York, CREST, United States

^d Graduate Center of City University of New York, United States



ARTICLE INFO

Article history:

Received 4 September 2014

Received in revised form 4 January 2015

Accepted 8 January 2015

Available online 13 February 2015

Keywords:

VIIRS

SST clear sky mask

Thermal fronts

ABSTRACT

Discriminating clear-ocean from cloud in the thermal IR imagery is challenging, especially at night. Thresholds in automated cloud detection algorithms are often set conservatively leading to underestimation of the Sea Surface Temperature (SST) domain. Yet an expert user can visually distinguish the cloud patterns from SST. In this study, available pattern recognition methodologies are discussed and an automated SST Pattern Test (SPT) is formulated. Analyses are performed with SSTs retrieved from the Visible Infrared Imaging Radiometer Suite (VIIRS) sensor onboard S-NPP using the NOAA operational Advanced Clear-Sky Processor for Oceans (ACSPo) system. Based on the analyses of global data, we have identified spatial features potentially useful for discriminating cloud from clear-ocean. The SPT attempts to mimic the visual perception by a human operator such as gradient information, spatial connectivity, and high/low frequency discrimination. It first identifies contiguous areas with similar features, and then makes a decision based on the statistics of the whole region, rather than on a per pixel basis. The initial objective of the SPT was to automatically identify clear sky regions misclassified by ACSPO clear sky mask as cloudy, and improve coverage in dynamic areas of the ocean and in the coastal zones. Future work will be directed towards extending the SPT to also minimize cloud leakages, and redesigning the current ACSPO clear-sky mask making full use of pattern recognition approach.

© 2015 Elsevier Inc. All rights reserved.

1. Introduction

Determination of Sea Surface Temperatures (SST) from satellite infrared sensors such as the Visible Infrared Imaging Radiometer Suite (VIIRS) requires a highly accurate scene identification. On the one hand, residual sub-pixel or ambient cloud ("cloud leakages") may corrupt SST product. On the other hand, clear-sky areas may be erroneously excluded from SST domain ("false alarms") causing data voids in some interesting areas of the ocean, often over long periods of time. VIIRS sensor is currently flown on board the Suomi National Polar-orbiting Partnership (S-NPP) platform launched on 28 October 2011. It will also be on board two follow-on Joint Polar Satellite System (JPSS) satellites, J1 and J2, planned for launch in 2017 and 2023, respectively.

The clear-sky mask for the NOAA Advanced Clear-Sky Processor for Oceans (ACSPo) VIIRS product employs comparisons of retrieved SST with a first guess SST, reflectance thresholds, and spatial uniformity tests (Petrenko et al., 2010). The version of ACSPo tested here uses the daily Canadian Meteorological Centre CMC product (Brasnett, 2008),

interpolated from 0.2° CMC grids to VIIRS pixels, as a reference. The ACSPo clear-sky mask (ACSM) generally performs well on a global scale, but tends to over-screen some highly dynamic areas with strong currents, cold upwellings, and eddies, as well as some coastal zones. There is no easy fix to this conservative nature of the ACSM within its current conceptual framework, e.g. by a simple adjustment of its thresholds, without triggering massive cloud leakages. Although the ACSPo SST domain tends to be larger than in similar SST products produced by NOAA partner organizations, our primary motivation was to further minimize ACSM false alarms in those interesting ocean regions, and more fully realize the potential of high-resolution (0.75 km at nadir), superior radiometric quality VIIRS imagery (e.g., Hillger et al. (2013, 2014), Seaman et al. (2014)) using the pattern recognition approach. Note that the same methodology can also be explored to minimize the cloud leakages, and otherwise improve or even redesign the ACSM. Work is currently underway to explore this potential.

Visual inspection of the retrieved SST in typical clear sky ocean regions, misclassified by the ACSM as cloud, suggests that such problematic areas are typically contiguous, with well-defined boundaries, and often located in the vicinity of ocean thermal fronts. Identification of such areas falls under the category of mathematical problems generally referred to as image segmentation. The subject of image segmentation has been of great interest to the image processing community for decades and a number of methods have been developed (Jain & Dubes,

* Corresponding author at: City College of New York, CREST, United States.

E-mail addresses: gladkova@cs.ccny.cuny.edu (I. Gladkova), yury.kihai@noaa.gov (Y. Kihai), alex.ignatov@noaa.gov (A. Ignatov), fshahriar@gc.cuny.edu (F. Shahriar), boris.petrenko@noaa.gov (B. Petrenko).

1988; Jain et al., 1999). Determination of ocean thermal fronts is also a well-studied area, which has been extensively explored with SST imagery (Belkin & O'Reilly, 2009; Cayula & Cornillon, 1992, 1995; Miller, 2009; Ullman & Cornillon, 2000). Note that customary practice is to analyze thermal fronts under clear sky conditions, after having the cloudy pixels removed. However, non-uniform scenes associated with ocean fronts and coastal zones, are typically the most challenging for the current clear sky masks including the ACSM, often leading to misclassification of cold water spots adjacent to thermal fronts as cloud, and thus limiting the ability of thermal front detection in clear-sky SST imagery.

This study aims to work around this vicious circle and incorporate an automated pattern recognition algorithm into clear sky mask. The proposed algorithm attempts to mimic some intuitive visual perception of SST imagery by a human eye and help distinguish typical uniform and contiguous ocean patterns from ragged structures typical of clouds. Even when the ocean is dynamic, it exhibits slow-meandering and swirl-like contiguous patterns. Difference between ocean and cloud patterns is more pronounced in the SST gradient magnitude domain. Viewed as a terrain, the dynamic areas of the ocean appear as sharp mountain ridges (corresponding to ocean thermal fronts) towering over flat valleys (corresponding to slowly changing ocean temperatures). In the proposed SST Pattern Test (SPT), we first identify such SST gradient ridges and adjacent contiguous areas with similar SST values, and then make ocean versus cloud decision based on the statistics of the whole region, rather than on a per pixel basis.

The analyses are performed with ACSPO SSTs derived from destriped VIIRS radiances. Note that destriping is critically important for this type of approach, because striping leads to artifacts in the gradient field, causes spatial discontinuities, and affects the statistics of high frequency components. Here, we use a destriping approach (Bouali & Ignatov, 2014) that was specifically developed for the use with VIIRS data and which is currently tested in the NOAA ACSPO operations. Furthermore, special pre-processing of VIIRS bow-tie areas was required before the SPT algorithm can be applied. It was developed in the course of this study and described in Section 2.3 below.

The current implementation of the SPT algorithm does not use any information other than patterns in the VIIRS retrieved SST field. In particular, albedo channels in the daytime data are very informative, but at this stage they were reserved for an independent verification of the algorithm. This is intentional and aimed at facilitating the desired consistency and continuity at day-night transition. Most importantly, at the initial stage of the algorithm development, the primary objective was to concentrate on the pattern recognition concept and fully explore its complementary potential to the current ACSM. Once the SPT algorithm

is implemented and tested with ACSPO VIIRS, it will be also included in ACSPO MODIS and AVHRR processing.

2. Approach

We first describe the proposed approach conceptually, leaving technical details and practical considerations for the follow-on Sections 2.1–2.3. The steps of the algorithm are demonstrated using a representative example of ACSPO misclassification of two types: “false alarms” (i.e., clear sky regions that have been mistakenly identified as “cloud” by the ACSM), and “cloud leakages” (i.e., clouds missed by the ACSM). This study focuses on false alarms and does not discuss cloud leakages.

A case study from the VIIRS granule acquired on 16 February 2013 from 22:00–22:10 UTC was selected to demonstrate the proposed approach. Retrieved SST values in all pixels of the selected scene are shown in Fig. 1a, and with the ACSM overlaid in Fig. 1b. There are three false alarms in this scene (circled in red). Two are found in the coastal zones, one in the Kagoshima Bay and the other around the Tanegashima Island. A third false alarm is found in a dynamic region to the south of the Yakushima Island, where different masses of water mix in a swirly pattern. There are also two cloud leakages (circled in blue). Those are beyond the scope of this study and will be analyzed later.

Unlike a human operator, automated cloud detection algorithms such as the ACSM, may misclassify the dynamic ocean as cloud. Recall that the human eye does not perceive absolute pixel values, but instead relies on the local contrasts, ratios, and gradients in an image. To illustrate this, the magnitude of the gradient field is shown in Fig. 2. The sharply-defined strands of SST gradient are likely thermal fronts on the ocean surface while the less regular mixed patterns of high and low gradients are associated with clouds. The proposed SST Pattern Test (SPT) explores the gradients and their lower order local statistics to resolve this misclassification in the ACSM and comprises the following steps (illustrated in Fig. 3):

Step 1: Narrow down the search domain.

Pattern recognition algorithms are computationally expensive and the search domain should be first narrowed down, by removing the most obvious cloudy regions while keeping in the analysis all potential “clear-sky” pixels. In our implementation, this was accomplished by excluding pixels satisfying at least one of the following conditions:

$$\begin{aligned} \text{SST} < 270 \text{ K}, \\ \text{Gradient magnitude} > 1 \text{ K}, \end{aligned}$$

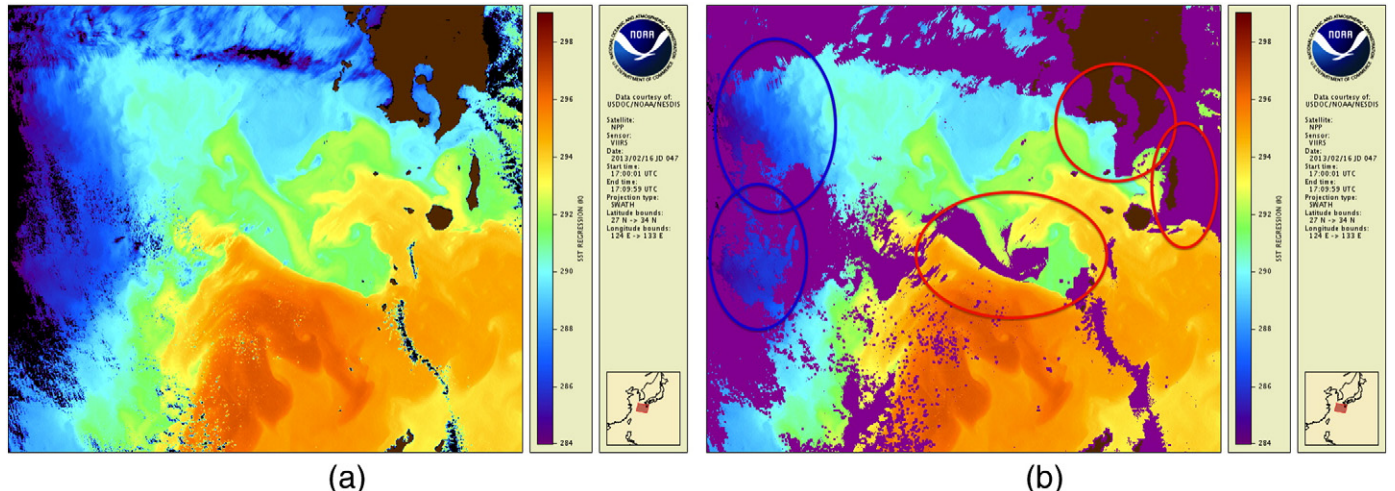


Fig. 1. East China Sea, 16 February 2013, 22:00–22:10 UTC (night). Land rendered in brown, ACSM cloud pixels in magenta and pixels with out-of-scale cold SST values in black; (a) VIIRS SST (without mask); and (b) VIIRS SST with ACSM overlaid.

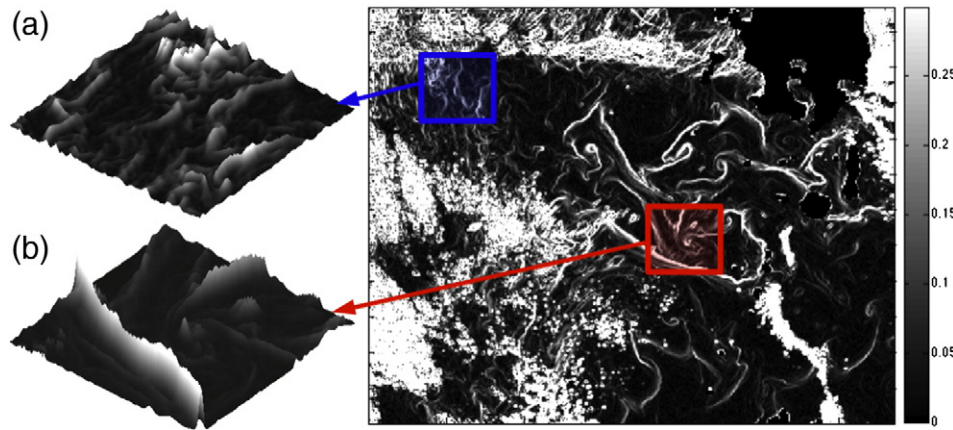


Fig. 2. SST gradient magnitude. Blue rectangle: cloud leakage; red rectangle: false alarm.

$$\Delta SST = \text{retrieved SST} - \text{reference SST} < -15 \text{ K},$$

Local standard deviation of Laplacian > $1/3$ K.

Fig. 3a confirms that Step 1 successfully eliminates many “ACSM cloudy” pixels. At the same time, it keeps the “warm clouds” (including false alarms circled in red in **Fig. 1b** as well as the cloud leakages circled in blue) in the search space. The following Steps 2–5 are performed only within this restricted domain.

Step 2: Determine SST gradient ridges (SGR).

Identification of the SGRs is a major component of the algorithm. Formally, the notion of SGR employed in this study is similar, but not identical to the ocean thermal front used in the literature (e.g. Cayula & Cornillon, 1992; Miller, 2009; Belkin & O'Reilly, 2009). The SGR is a more general term inclusive of thermal fronts. The ACSPO SST field analyzed at this step still represents a mix of true SST and cloud (except for the most obvious cloud excluded at Step 1). As a result, the identified SGRs may also include, in addition to ocean thermal fronts (i.e., the curves separating two different water masses), boundaries between clear sky and thin cloud, and quasi-linear textures of (e.g. cirrus) cloud/cloud transition overlaying highly variable SST field. The SGRs detected by our algorithm are shown in **Fig. 3b**. More details of the SGR detection algorithm are given below in [Section 2.1](#).

Step 3: Determine spatially connected regions with retrieved SST colder than the reference SST.

This step is accomplished using an image processing segmentation procedure applied to $\Delta SST = \text{retrieved SST} - \text{reference SST}$. The purpose is to find contiguous regions with ΔSST below the specified threshold. It is those clear areas that are most often misclassified by the ACSM as cloud. Various types and implementations of segmentation procedure do exist in any standard programming language, with a wide range of the required computational resources, depending on the objective and desired accuracy (Jain & Dubes, 1988; Jain et al., 1999). We use a watershed algorithm (Beucher, 1982; Couprie & Bertrand, 1997; Vincent & Soille, 1991) applied to ΔSST . There are different implementations of the watershed approach, including watershed by flooding, topographic distance, inter-pixel watershed, and optimal spanning forest algorithms. The one used in this study is the watershed by flooding. Its principle can be illustrated by viewing the image of ΔSST as a topographic relief, where the gray level of a pixel is interpreted as its altitude. A drop of water falling on a topographic relief flows along a path to finally reach a local minimum. Intuitively, the watershed corresponds to the limits of the adjacent catchment basins. **Fig. 4a** and **b** maps ΔSST as a false color image and as a topographic relief, respectively. The “water” level in the watershed interpretation was set to $\delta_0 = -1$ K in **Fig. 4b**.

In our application, the over-segmentation is acceptable and actually preferred over the under-segmentation scenario, when a mix of clear sky and cloudy pixels appears in the same segment. Since the decision is made on a per-cluster basis, we require segments to be large enough to be considered as a potential ocean pattern. We use 100 pixels as a lower bound for the segment size (approximately equivalent to a 10 by 10 km region). Segments identified by segmentation procedure, are shown in **Fig. 3c** where the distinct contiguous segments are rendered in different colors.

Step 4: Ridge Adjacency Test.

As mentioned earlier, the ACSM false alarms often occur in dynamic ocean areas with strong currents, cold upwellings and eddies. This is primarily due to the fact that the clear sky ACSM tests rely on the reference SST field which can be substantially different from the instantaneous retrieved SST values. The spatial uniformity test may also contribute, but its robust implementation in ACSPO minimizes false alarms. Visual analysis of typical ACSM misclassifications suggests that most of such false alarms take place in the proximity of ocean thermal fronts and often correspond to retrieved SST being colder than the reference SST. Therefore, the segments with negative ΔSST adjacent to SGRs are considered as potential risk regions for the ACSM misclassification. The purpose of this step is to check which segments are adjacent to SGRs and labeled as cloudy by ACSM. **Fig. 3d–e** as compared to **Fig. 1b** shows that the spots misclassified by the ACSM as cloud, are adjacent to fairly long portions of the ridges found in Step 2. There are also some clouds adjacent to SGRs. However, four such segments circled in **Fig. 3e** are all adjacent to very short ridges. As a result, the SPT may add new cloud leakages to those already present in the ACSM. To prevent these new cloud leakages, one can increase the minimum number of pixels in the SST Local Ridge Test. In the current implementation, it is set to 10, which may not be sufficient to confidently decide whether or not the region adjacent to a short ridge is ocean or cloud. On the other hand, increased threshold may lead to losing some small cold spots of the ocean, especially in the coastal areas, where many ACSM false alarms are found. The following Tests for corner cases were added to identify and reject potential SPT cloud leakages.

Step 5: Tests for Corner Cases

Many cold clouds are eliminated at Steps 2–4, and yet, some may go uncaptured (cf. **Fig. 3e**). Also, there are cases when the segmentation procedure fails to separate cloudy and clear pixels, leaving them in one cluster. In such cases, the whole segment adjacent to the ridge would be accepted as “clear sky”. Another scenario is when a short SGR corresponds to a flaky cloud boundary, rather than to an ocean thermal front. Such cases prove difficult even for visual identification from the VIIRS SST field alone. However, identification can be improved when the texture (context) of the surrounding

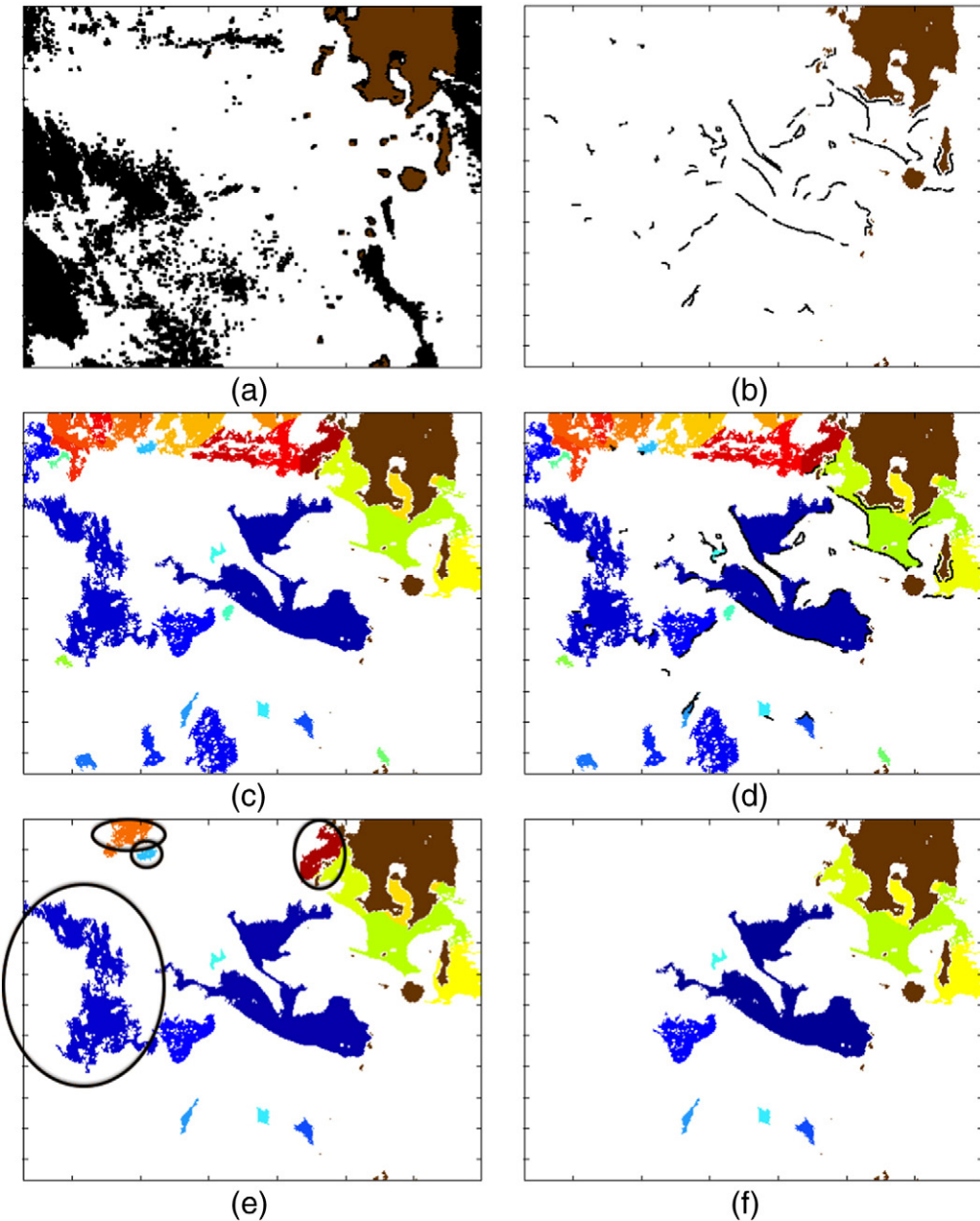


Fig. 3. Steps of the SST Pattern Test (SPT); (a) Step 1: Search over white pixels only; (b) Step 2: SST gradient ridge (SGR) test; (c) Step 3: Spatially-connected segments; (d) Step 4a: Segments with overlaid SGRs; (e) Step 4b: Clouds adjacent to SGRs; (f) Step 5: Rejecting corner cases.

zones is considered, on a larger scale. Detailed description of our implementation is found below in Section 2.2.

Finally, the output of the SPT is only applied to those pixels excluded by the ACSM as cloudy, and the resulting pixels are restored back into the SST domain. Currently, no change is made to the ACSM “clear sky” pixels, even though the SPT output may suggest that they are cloudy. Note that this restorative nature of the SPT is due to our initial objective, to extend the ACSPO SST domain by including the interesting open ocean areas with strong dynamics, and the coastal zones, and meet the most immediate need of the NOAA SST users.

2.1. Identification of SST gradient ridges (SGR)

SGRs can be viewed as proxies of ocean thermal fronts, which are usually detected using two standard approaches. One class of algorithms

employs gradient-based edge detection approach, such as Sobel, Prewitt, Canny etc. (Roushdy, 2006). These algorithms are generic to any natural imagery and have been extensively used for front detection in chlorophyll and SST imagery (Belkin & O'Reilly, 2009). The other class of algorithms is population-based (Cayula & Cornillon, 1992, 1995; Ullman & Cornillon, 2000). These algorithms assume that the SST probability density in the vicinity of thermal fronts is bimodal, with two distinct modes corresponding to different masses of water. Our algorithm builds on the heritage of both and employs the gradients of the SST field and the local SST statistics.

Visual inspection of Figs. 1 and 2 suggests that the SST gradient magnitudes viewed as a terrain look like sharp ridges, whereas the adjacent clear sky ocean areas look like valleys. The notion of ridges and valleys in digital image processing was introduced in Haralick (1983) to represent a set of curves connecting points of local maxima (ridges) and minima (valleys). The SGR notion used in this study additionally requires

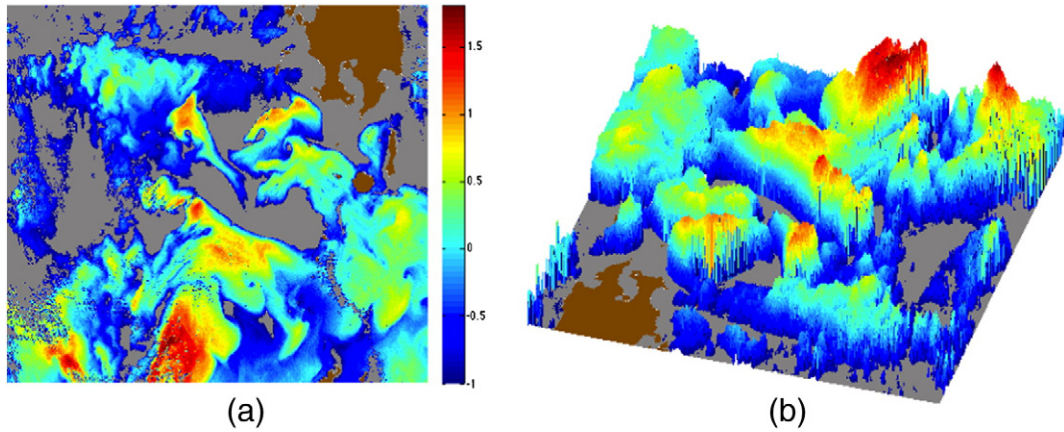


Fig. 4. (a) ΔSST = retrieved SST – reference SST; (b) ΔSST as a topographic relief (rotated for improved visual perception). Areas with $\Delta\text{SST} < -1$ K (corresponding to starting flooding level) are rendered in gray.

that the SST gradient magnitudes be small on the either side of the ridge (cf. Fig. 2).

The block diagram of the SGR identification is shown in Fig. 5. It receives the retrieved and reference SST's, the search domain (output of Step 1), and a set of parameters (defined below in this section) as input, and returns a structured array with SGRs on the output. All blocks of the diagram, except for the SST Local Ridge Test, utilize standard procedures, such as dilation, erosion, morphological thinning and connected components.

First, the binary mask M_{δ_0} is defined for all pixels with $\Delta\text{SST} < \delta_0$ ($\delta_0 = -1$ K in this implementation, cf. Fig. 6a). Second mask, \tilde{M}_{δ_0} , is obtained from M_{δ_0} by its erosion and subsequent dilation (cf. Fig. 6b), to identify the portions of the M_{δ_0} 's boundary that are sensitive to morphological opening. The cloud boundaries tend to be more jagged and thus will change as a result of this morphological operation, whereas the

ocean thermal fronts are more stable and smooth, and thus will survive this operation. Contours C_{δ_0} of M_{δ_0} , and \tilde{C}_{δ_0} of \tilde{M}_{δ_0} are shown in Fig. 7. Their multiplication results in a new binary mask, which is set to 1 along the stable portions of the boundaries, and to 0 elsewhere. The output is shown in Fig. 8. A 5-by-5 square structuring element was used for both morphological operations to obtain \tilde{M}_{δ_0} and a 3-by-3 square structuring element for erosion to obtain both contours C_{δ_0} and \tilde{C}_{δ_0} .

The next step of the algorithm is the SST Local Ridge Test. It may be computationally expensive if the number of search pixels is large. This justifies the step of morphological thinning, which outputs a skeleton S with a width of 1 pixel and thus significantly narrows down the search domain. The test is performed for every pixel in S using a local $w \times w$ window w ($w = 41$ in the current implementation). The purpose of this step is to eliminate pixels at the ocean/cloud and cloud/cloud

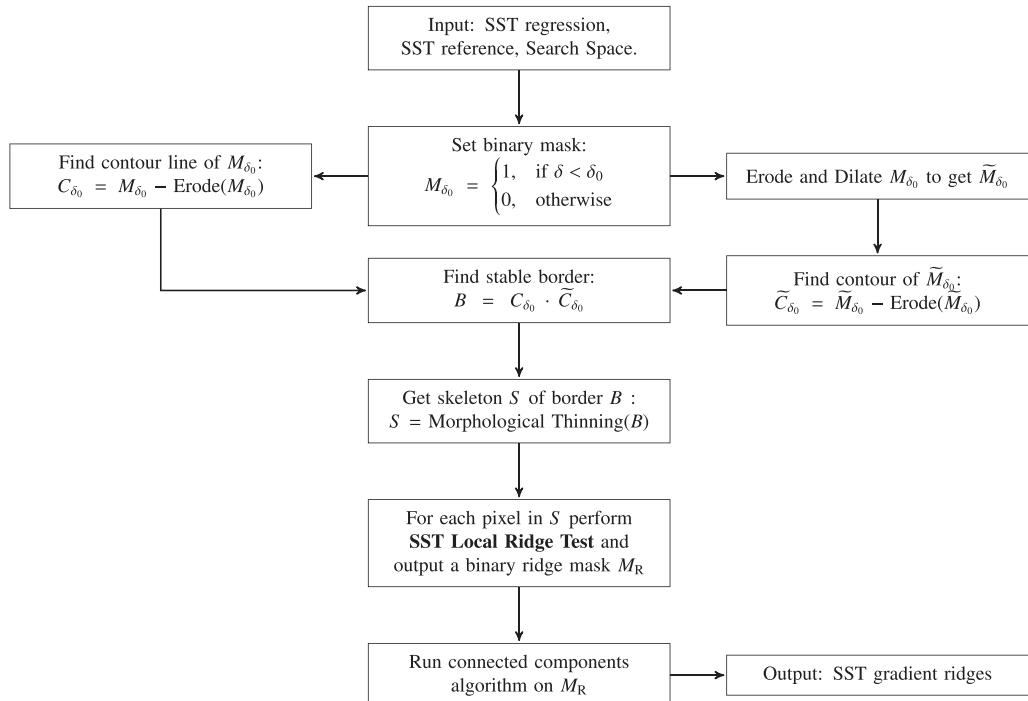


Fig. 5. Block diagram of Step 2: SST gradient ridges.

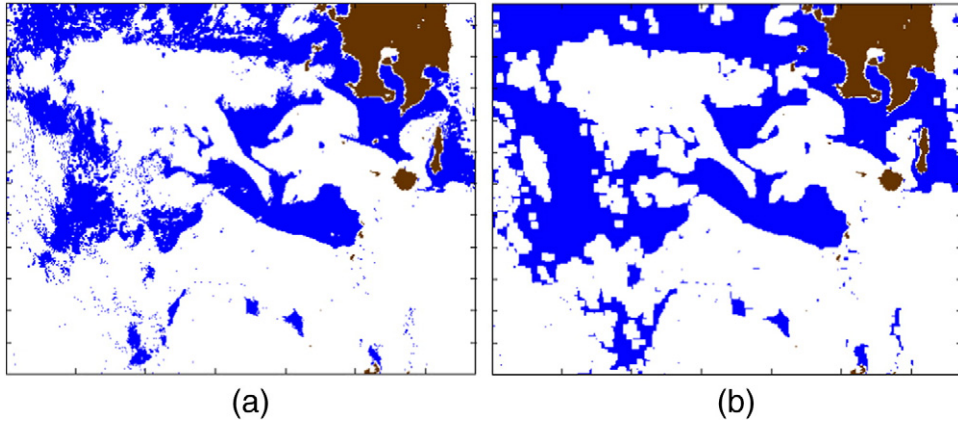


Fig. 6. (a) Binary mask M_{δ_0} . Blue pixels correspond to $\delta < \delta_0 = -1$ K; (b) Binary mask \tilde{M}_{δ_0} , obtained by erosion and dilation of the mask M_{δ_0} .

boundaries. Visual inspection of the gradient magnitude image (cf. Fig. 2) suggests that the average gradient on either side of the thermal front is relatively small. We therefore compute two mean gradients, μ^T and μ^F , and test if they both are below thresholds μ_0^T and μ_0^F , respectively. The superscript “T” (true) is used to represent pixels which belong to the set defined by mask M_{δ_0} and “F” (false) represents pixels outside of that set. Additionally, the standard deviation over the full local window w (excluding the local ridge) is calculated and checked if it is below a threshold, σ_0^w . These first and second order statistics effectively eliminate most ocean/cloud and cloud/cloud boundary pixels. Fig. 8 shows in blue the pixels of S that fail the Local Ridge Test, whereas the SGRs surviving the test are shown in red. Note that SGRs are rendered in thicker lines, for the purpose of visualization. In the current implementation, the parameters μ_0^T , μ_0^F , and σ_0^w are all set to 0.3 K, which was determined experimentally, but there is a provision in the code to specify those three different thresholds.

In summary, the steps of the SST Local Ridge Test for each pixel $p \in S$ are as follows:

1. Locate a window w centered around pixel p .
2. Find all pixels p in the local window covered by the mask M_{δ_0} and not including the border B :

$$P^T = \{p \in w | p \in M_{\delta_0}, p \notin B\}.$$

3. Find all pixels p in the local window outside the mask M_{δ_0} and outside

the border B :

$$P^F = \{p \in w | p \notin M_{\delta_0}, p \notin B\}.$$

4. Compute:

$$\sigma^w = \text{standard deviation of gradient magnitude over } P^T \cup P^F.$$

$$\mu^T = \text{average gradient magnitude over } P^T.$$

$$\mu^F = \text{average gradient magnitude over } P^F.$$

$$M_R = \begin{cases} \text{True, if } \sigma^w < \sigma_0^w, \mu^T < \mu_0^T, \mu^F < \mu_0^F; \\ \text{False, otherwise.} \end{cases}$$

The last block of the SGR algorithm is the determination of the connected components of the M_R . We use the 8-adjacency connectivity and discard the components with less than 10 pixels (i.e. fragments shorter than ~ 10 km).

Note that the computation of the gradients in an SST image requires numerically accurate partial derivatives. The artifacts inherent to the retrieved SST field make the output of the standard numerical differentiation procedures, such as divided difference, unusable. Alternative solutions are: fitting polynomial approximations (Haralick, 1984) smoothing with a (truncated) Gaussian filter (Meer & Weiss, 1992) and kernel based differentiation (Farid & Simoncelli, 2004; Gonzalez & Woods, 1992). Customarily, the Sobel kernel is employed to compute the gradient with smoothing, but the result was found to be too noisy for our application. In our implementation, the 5-point linear-phase separable kernel derived for differentiation of discrete multidimensional signals (Farid & Simoncelli, 2004) was used.

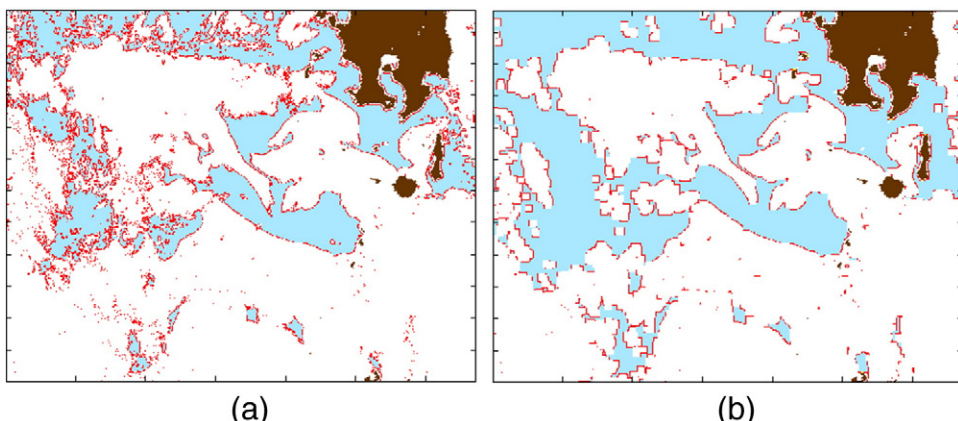


Fig. 7. (a) Contour line C_{δ_0} (red) of the mask M_{δ_0} (cyan); (b) Contour line \tilde{C}_{δ_0} (red) of the mask \tilde{M}_{δ_0} (cyan).

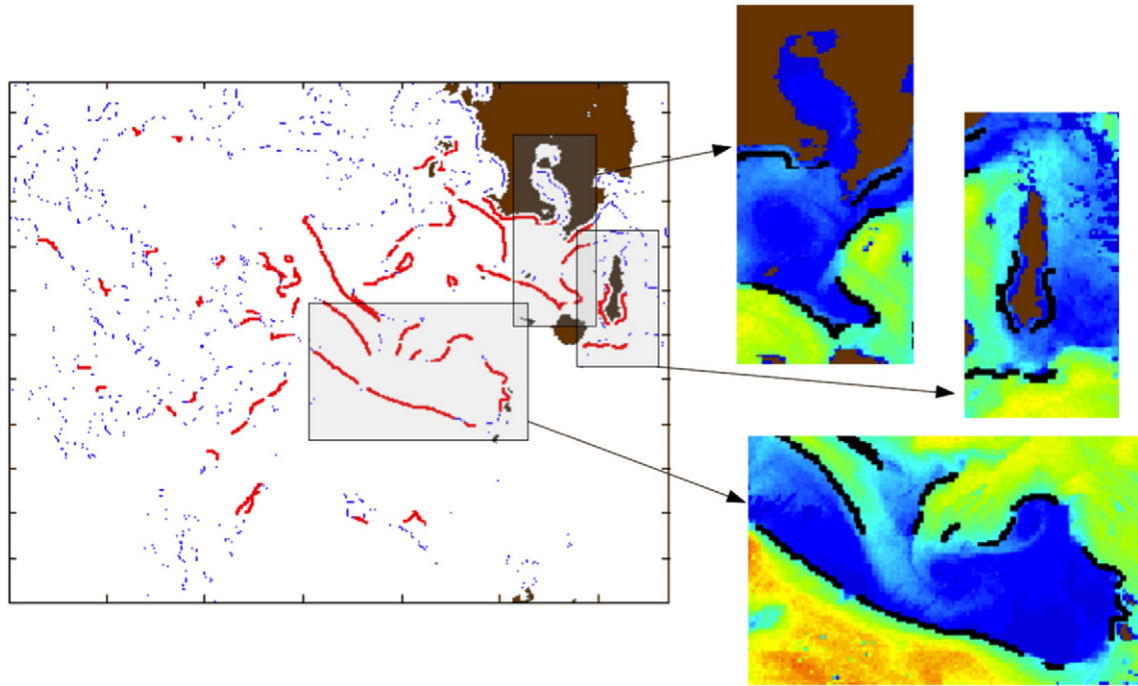


Fig. 8. Skeleton S (blue) overlaid by SST gradient ridges (thick red). Areas of the three ACSM false alarms in Fig. 1 are shown on the right overlaid with Δ SST.

2.2. Handling corner cases in the current SPT implementation

The current implementation of the SPT Steps 1–4 may not be fully complete or optimal. In particular, some difficulties may arise in processing complex cases such as the low warm clouds (especially at night), clouds overlapping ocean dynamic features or even other clouds. Such situations may lead to SPT leakages and false alarms. Recall that our initial objective was to confidently restore at least some clear pixels, misclassified as cloud by the ACSM, and demonstrate the potential of the SPT. At this stage, the goal was to absolutely minimize additional SPT cloud leakages (even at the expense of a larger rate of remaining ACSM “false alarms”). With this in mind, several additional tests have been implemented, to minimize some remaining (or even potential) SPT leakages. Those include:

1. Segment Stability;
2. Relative length of SGR to total segment border;
3. Jaggedness of the segment border.

If one of these tests fails, the pixels in the corresponding cluster will not be reclassified from cloudy to clear.

2.2.1. Segment Stability

This test makes use of the fact that clouds typically have a more complex geometric shape than oceanic features. One measure of this complexity is a change in the area covered by a segment during morphological variations. In the current implementation, the additional advantage was taken of the results of morphological operations, erosion and dilation, generated at the SGR step. Here, two binary masks, M_{δ_0} and \tilde{M}_{δ_0} , are applied to only those segments surviving Step 4, and the difference between the numbers of pixels in the original and morphed segments is calculated. Figs. 6 and 7 confirm that clouds are very sensitive to the morphological variation. Segments that change by > 20 % are rejected.

2.2.2. Relative length of SGR to total border

Short SGRs may belong to relatively small areas of cold upwellings or eddies which should be preserved. However, some other short SGRs may also be adjacent to large cloudy segments. To minimize SPT leakages, the ratio of the gradient ridge to the total border length is computed, and the segment is rejected if this ratio is < 10 %.

2.2.3. Jaggedness of segment border

Usually, the cloud edges are jagged as opposed to smooth SST fronts. We apply the Gaussian filter to the binary mask of the segment to smooth out its border and then compute the ratio of the original/smoothed lengths. Segments that change by > 70 % are rejected.

These “corner cases” tests do minimize SPT cloud leakages. The plan is to implement the current SPT into ACSPO operations, accumulate representative statistics, and identify features useful for their automatic identification and exclusion. Next, we plan to revisit the current SPT and add a new ocean front product in ACSPO, which minimizes the number of corner cases. Finally, our analyses strongly suggest that the SPT performance can be further improved, if used in conjunction with other clear-sky tests, such as those currently implemented in the ACSM.

2.3. Bow-tie areas

The pattern recognition algorithm uses local spatial characteristics of the SST field, and requires that the underlying 2D SST surface is continuously differentiable. This requirement is not satisfied for the VIIRS imagery in the original swath projection (Hillger et al., 2014). As a result, the performance of the SPT degrades towards bow-tie areas, and the zones with deleted pixels cannot be processed. Destriping helps minimize unidirectional artifacts in the VIIRS imagery, but not the geometric distortions. A schematic of the VIIRS half-scan (from nadir to swath edge) is shown in Fig. 9. Without the bow-tie effect, each half-scan would be represented by the blue shaded area. Pixels outside of this area overlap with the adjacent scans. Radiance data in the red pixels are deleted on board SNPP before transmitting to the ground and

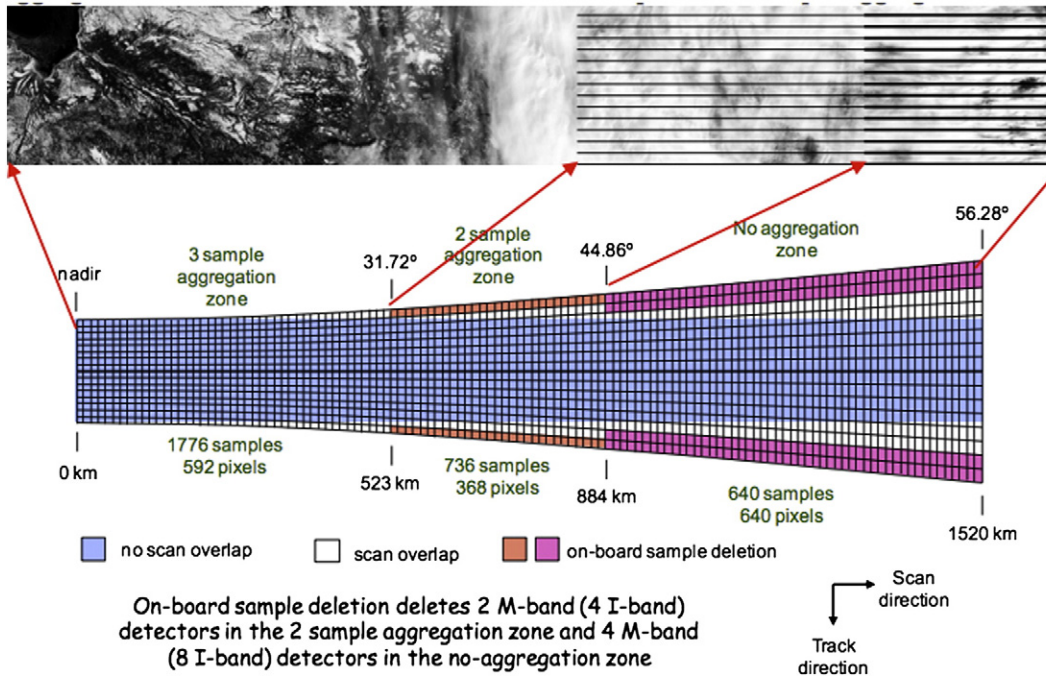


Fig. 9. (Reprinted from VIIRS Sensor Data Record (SDR) User's Guide (Cao et al., 2013), page 20): Top: Example of bow-tie deletion effect when the raw data is displayed in the original SDR swath projection. Bottom: Schematic of bow-tie effect, and deletion and aggregation zones for single-gain M-bands (note that the scale is exaggerated in the cross-track direction).

replaced in the VIIRS Sensor Data Records (SDR; Level 1) with fill value, in the interest of compression. Also, the VIIRS pixels are aggregated as 3:1 from nadir to scan angle 31.72° , 2:1 from 31.72° to 44.86° and remain unaltered at $> 44.86^\circ$.

There are two standard ways to handle the bow-tie affected areas: geographical remapping and resampling. Remapping may appear more intuitive for image processing. However, it is computationally more expensive and irreversible. This is why it is usually done at higher processing levels. Aggregating individual VIIRS pixels into grids would also alter the original swath data, and complicate the setting of the SPT clear/cloud bit in the ACSPO Level 2 product.

Resampling, on the other hand, does not have to be done on a fixed grid. Furthermore, it is reversible and computationally cheap. Note that, similarly to the original swath projection, the latitude spacing in resampled data may not be uniform and can cause the distortions of the gradient values. Resampling ensures topological continuity, which is critical for the SPT to correctly identify the positions of SGs and borders of the segments.

Keeping in mind the need of real time ACSPO Level 2 processing, per column resampling was tested and found acceptable. Fig. 10 shows the steps of the resampling algorithm. Latitude values for each column are first sorted and each column of the SST image is reordered accordingly. Fig. 10a and b shows the original SST image and the result of its reordering by latitude. More details are shown in Fig. 11a and b, for one particular column (marked in Fig. 10). Note that SST values in the overlapping intervals shown in Fig. 11b may not be identical, due to VIIRS radiometric and/or residual striping noise. The unique SST values in the overlapping intervals are calculated by smoothing with the median filter and then applying Gaussian interpolation in the fill zones. The result of resampling is shown in Figs. 10c and 11c.

We emphasize that resampling is an intermediate processing step here, which is only used in the SPT and does not affect the actual SST values reported in ACSPO granules. After the SPT is run, and corresponding SPT flag set, the per-column sorting order is reverted and the newly derived flag is appended to the original ACSPO Level 2 pixels. The SPT mask values computed in the deletion zones are discarded.

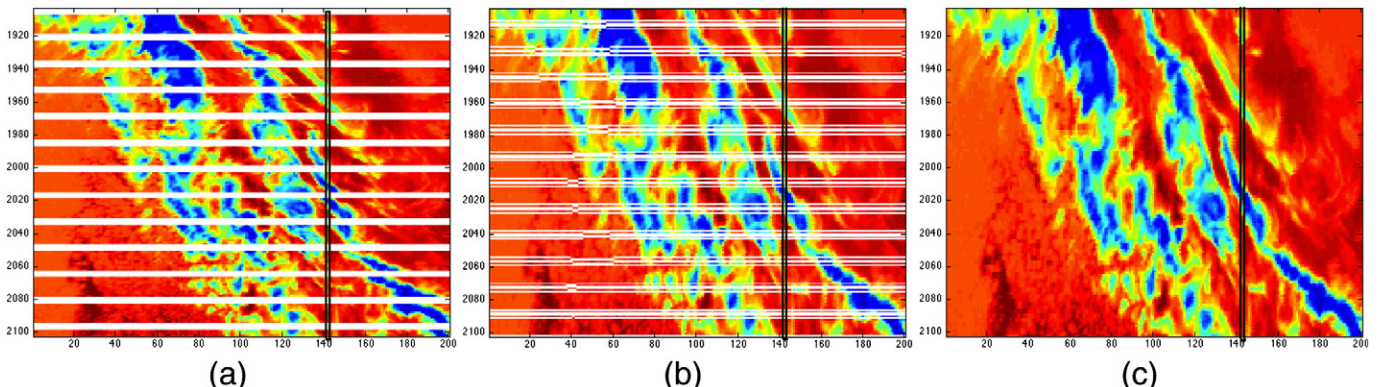


Fig. 10. Resampling steps: Example of bow-tie 200×200 crop (with row/column indexes preserved from the original ACSPO VIIRS granule); (a) original; (b) reordered; (c) resampled; the profile at column 141 is shown in Fig. 11.

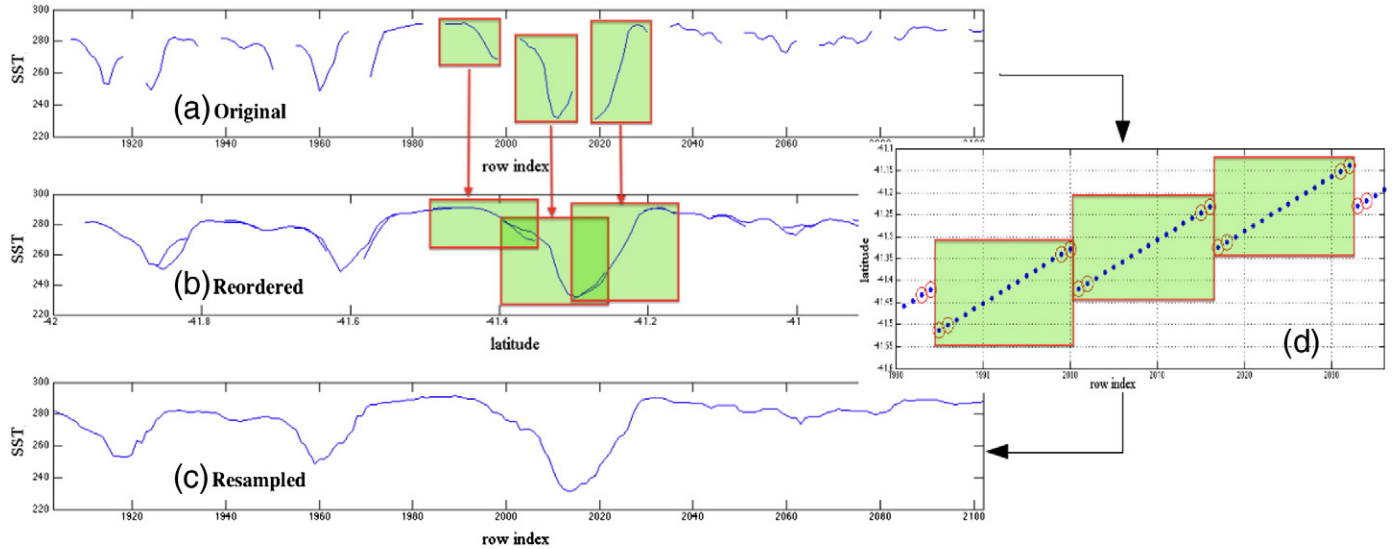


Fig. 11. Resampling steps for column 141 marked in Fig. 10. Latitudes for the three selected intervals are shown on the right insert. Circled points correspond to SST values in removed pixels (with fill radiance values).

Note that although the continuity of the first derivatives is preserved in the current resampling, the computed gradient magnitudes may degrade towards larger scan angles. Currently the same SGR threshold is used in the full swath. Future work may include defining view zenith angle specific thresholds.

3. Results

At the initial stage of the SPT development, 48 cropped images representative of typical ACSM misclassifications have been selected, visually inspected and hand-marked. This data set was used to train the

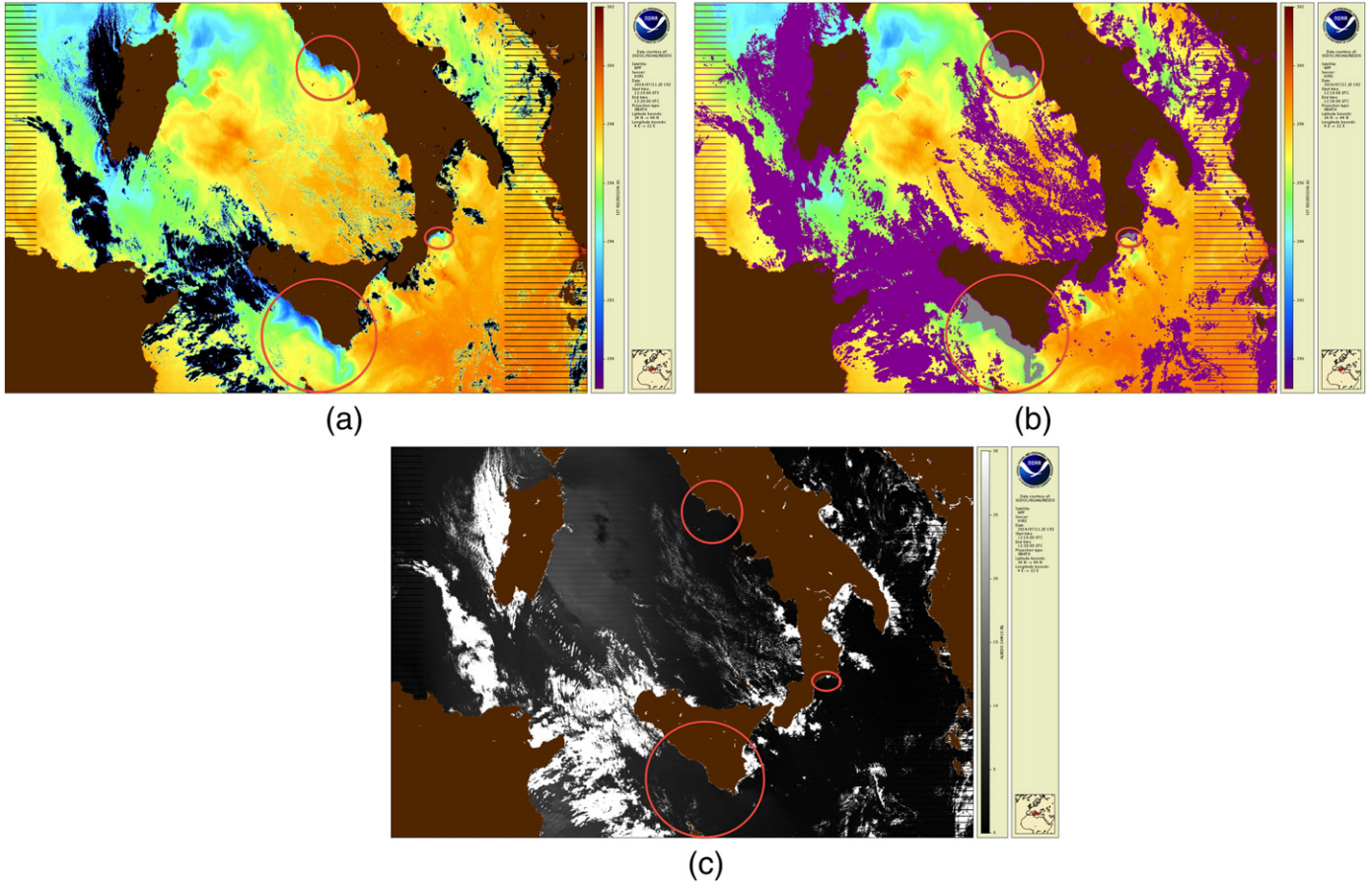


Fig. 12. Cold upwellings in the Mediterranean Sea on 11 July 2014 (day). Land rendered in brown and pixels with out-of-scale cold SST values in black. Magenta: the ACSM and SPT agree and say cloud. Gray: pixels restored by the SPT back in SST domain; (a) SST; No cloud mask; Cold upwellings are circled in red; (b) SST with cloud mask overlaid; SPT restored shown in gray; (c) VIIRS reflectance in band M10 centered at 1.61 μ m.

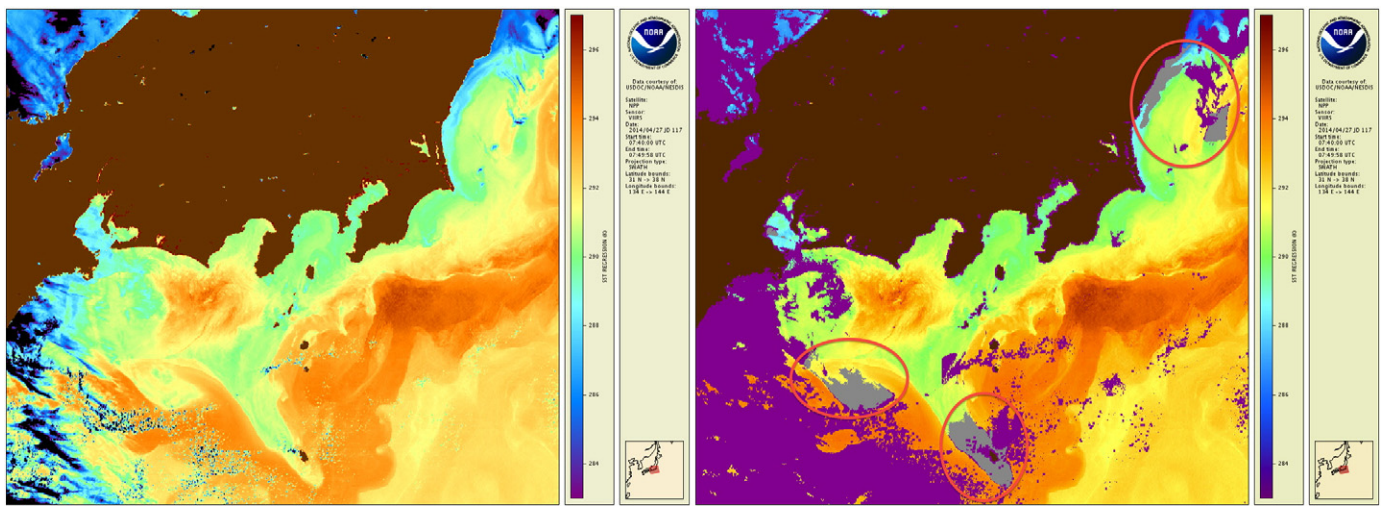


Fig. 13. Same as in Fig. 12 but for the Kuroshio Current in the vicinity of Honshu Island, on 27 April 2014 (day).

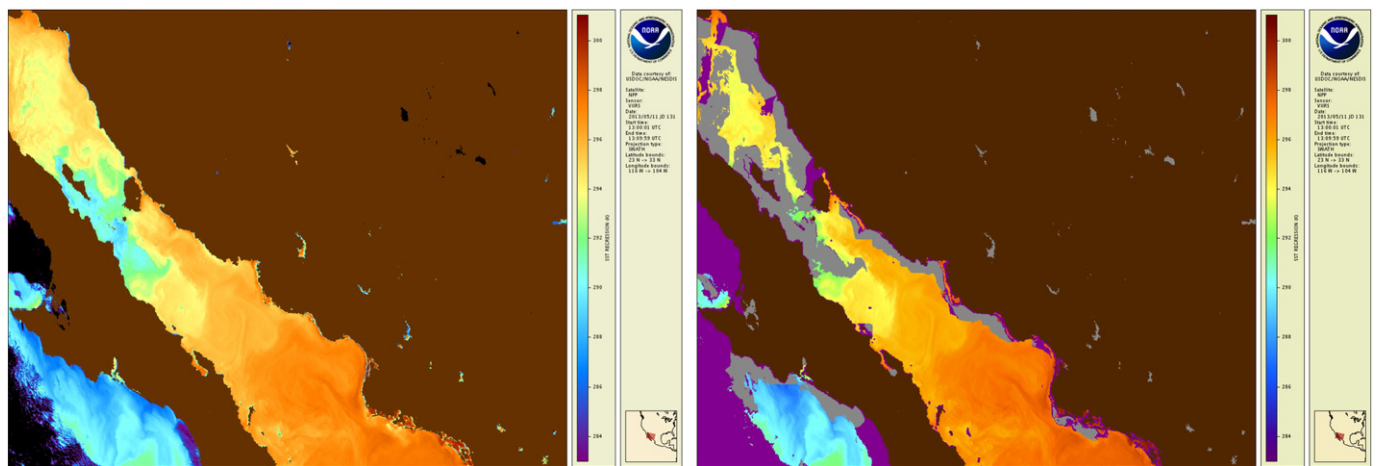


Fig. 14. Same as in Fig. 12 but for Gulf of California, on May 11, 2013 (night).

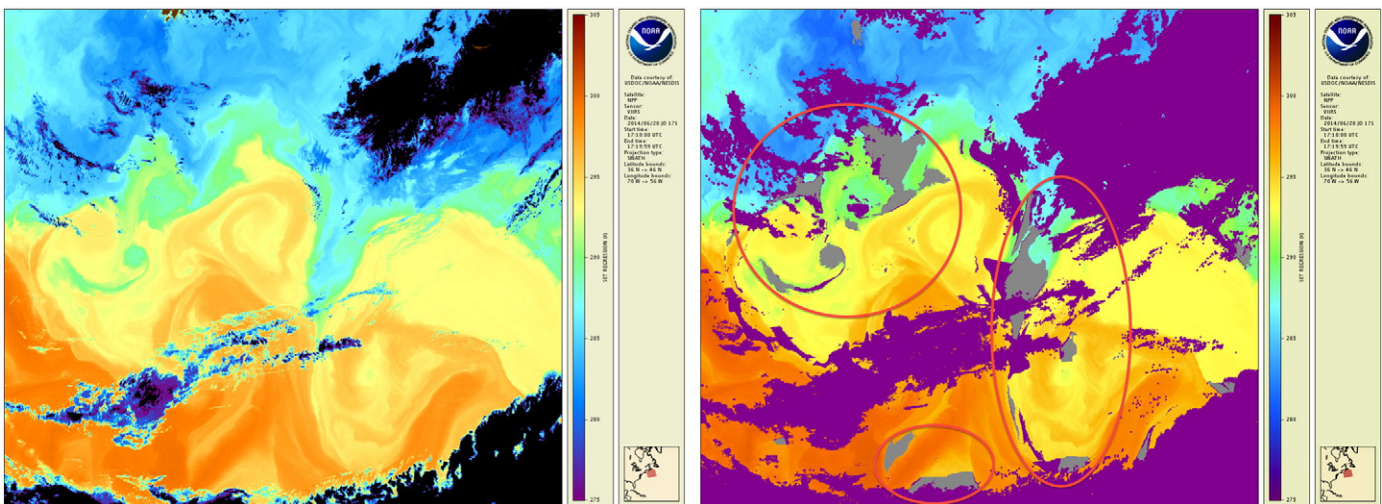


Fig. 15. Same as in Fig. 12 but for Gulf Stream on 20 June 2014 (day).

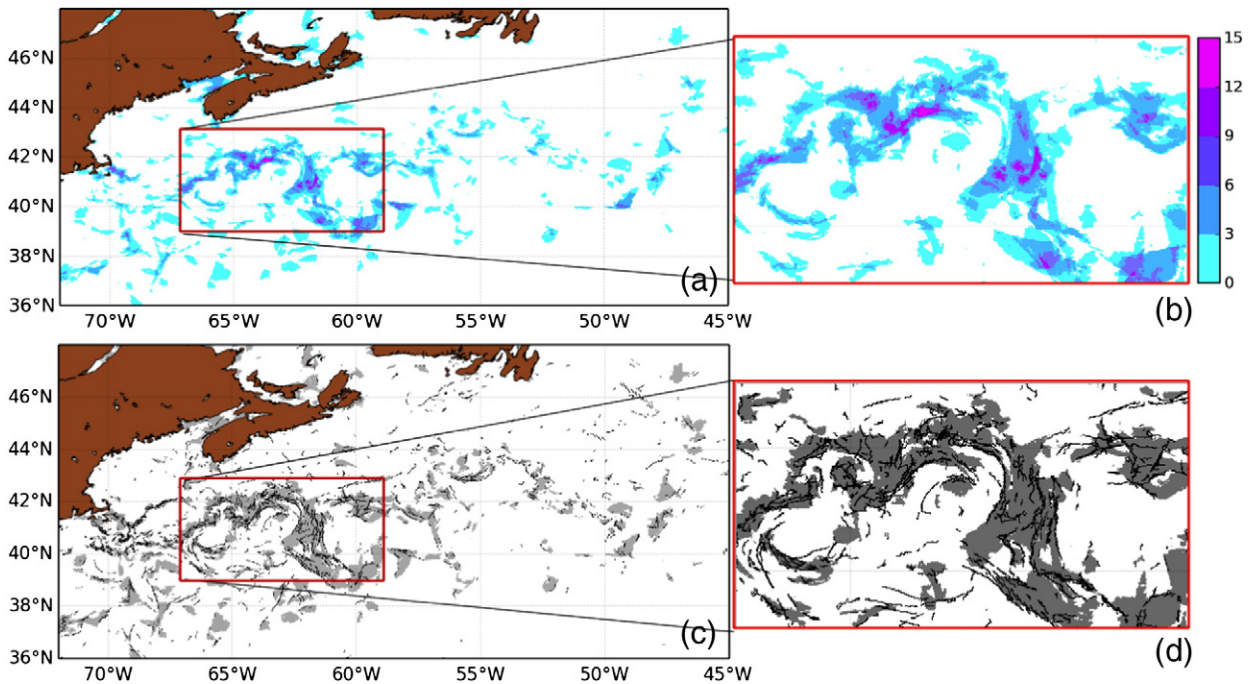


Fig. 16. Percentage of SPT restored pixels in the Gulf Stream area (77 ACSPO granules from 11 June–4 July 2014): (a) percent of SPT additions to the ACSM clear-sky domain; (b) zoom in the area of the Gulf Stream with the largest percent of ACSPO misclassifications and SPT restorals (note that the color-bar is quantized at 3%); (c-d) same as (a-b) but with SPT additions rendered in gray, and corresponding SGPs overlaid in black.

proposed algorithms, and evaluate SPT additions to the ACSM clear-sky domain. Initially, the SPT only processed the central zone of the VIIRS imagery (scan angle $\pm 31.82^\circ$). Following implementation of the resampling algorithm, the SPT processing was extended to the full VIIRS swath.

The SPT has been additionally tested using more than 600 10-min ACSPO VIIRS granules, including two days of global data in July 2014 (288 granules; recall that one full day contains 144 granules) and 3 weeks over the Gulf Stream area in June–July 2014 (77 granules). Other days and granules have also been analyzed, to ensure stability and reproducibility of the SPT performance in time. Below, typical examples of SST imagery and some statistical summaries for two data sets are discussed, including the global set (288 global granules from 10–11 July 2014), and the Gulf Stream (crop) sample which represents the most dynamic subset of the 77 regional granules collected from 11 June–4 July 2014 over the area from 39° to 43° N and 59° to 67° W.

An example daytime ACSPO SST image over the Mediterranean Sea on 11 July is shown in Fig. 12. Three upwellings — one off the west coast of Italy in the Tyrrhenian Sea (between Rome and Naples), the other off the south coast of Sicily in the Strait of Sicily, and the third off the south-east coast of Calabria in the Ionian Sea — are screened out by the ACSM, because they are colder than the reference SST and the ambient waters by $3\text{--}4^\circ$ C. The SPT successfully restores these areas back into SST domain. The corresponding reflectances in the VIIRS band centered at $1.61\text{ }\mu\text{m}$ (shown in Fig. 12c) and several SST images over the same area later in July (not shown) confirm that these sub-regions remained largely cloud free. The upwellings did show some minor evolution in time, but they largely remained in the same locations and retained comparable SST contrasts.

Fig. 13 shows an example of daytime SST imagery of the Kuroshio Current on 27 April 2014. This very dynamic area is characterized by high SST contrasts. Circled are the three largest regions restored by the SPT, one in the coastal Honshu and the other two areas offshore. The visual inspection of the SST patterns and comparison with corresponding measurements in the solar reflectance bands (not shown) confirm that the restored areas are indeed SST features and not cloud.

A night example of restoration in the coastal zone of the Gulf of California is shown in Fig. 14. Most of the coastal zone was misclassified by the ACSM. There are no corresponding measurements in the solar reflectance bands at night. However, comparison between the left and right images in Fig. 14 and analyses of the corresponding daytime and nighttime observations for several consequent overpasses, suggest that the restored areas are indeed SST features and not cloud.

A daytime image of the Gulf Stream, is shown in Fig. 15. This is an example of the ACSM misclassification in the glint area, where the performance of the clear sky mask usually degrades (e.g. Hutchison et al. (2005)). Fig. 15 suggests that even in this complex case, numerous pixels are successfully restored by the SPT.

Fig. 16 summarizes the geographical distribution of SPT restorals in the Gulf Stream area during the three weeks in June–July 2014. Fig. 16a and b shows that regionally, the SPT restores up to 15% of pixels misclassified by the ACSM as cloudy, into ACSPO clear-sky domain. Fig. 16c and d additionally shows that the ACSM tends to be progressively more conservative in the areas with the highest density of ocean fronts. This is exactly where the SPT is most needed and at the same time most useful.

Table 1 summarizes the ACSM and SPT performance statistics, over the globe and over the selected Gulf Stream crop. Globally, the ACSM identifies 18.35% of total ocean pixels as suitable for SST retrievals during the daytime, and 18.49% at night. The SPT additions are from 0.20% at night to 0.29% during the daytime. High percentage of clear sky SST pixels, remarkable consistency between day and night, and a relatively small fraction of the ACSM false alarms (i.e. SPT additions), confirm that overall the ACSM is a globally well tuned and balanced mask.

Over the Gulf Stream (crop) domain, the fraction of ACSM clear-sky pixels is 37.43% during the daytime and 32.47% at night. The increase of the clear-sky domain by a factor of ~ 2 from the global numbers is consistent with known cloud free bias in this area, during the local summer (Alliss & Raman, 1995). Note also that the day and night clear-sky fractions are somewhat out of balance, likely suggesting a more conservative ACSM screening at night, when reflectance bands are missing

Table 1

ACSM: Percent of clear-sky ocean pixels (relative to total ocean pixels). SPT: Increment in number of clear-sky pixels restored by the SPT. (In brackets, percent increase over the ACSM is shown.) For instance, for global set, the ACSM (day) provides 18.35% clear-sky pixels. The corresponding percent of clear sky SST pixels provided by ACSM + SPT combined, is $18.35\% \times 1.0029 = 18.40\%$.

	ACSM (day)	SPT (day)	ACSM (night)	SPT (night)
Global	18.35%	$\times 1.0029$ (0.29%)	18.49%	$\times 1.0020$ (0.20%)
Gulf Stream (restricted to 39°–43° N, 59°–67° W)	37.43%	$\times 1.0282$ (2.82%)	32.47%	$\times 1.0427$ (4.27%)

over this complex area. The SPT adds to the ACSM domain 2.82% during the daytime, and 4.27% at night. These additions are from $10 \times$ (day) to $20 \times$ (night) larger than the global average numbers. Note that these are the average numbers over the Gulf Stream area, but locally, the added domain may be as large as 15% as seen in Fig. 16b. Note also that the SPT restores more data at night, attempting to make up for the lack of day/night balance in the original ACSM. Yet, the ACSM + SPT fractions (38.5% during the daytime and 33.9% at night) remain out of balance, possibly due to the diurnal cycle of cloud coverage in the Gulf Stream area (Minobe & Takebayashi, 2014).

The major observation from Table 1 is that the SPT additions to the ACSM are highly non-uniform in space and in time. The ACSM tends to be more conservative in highly dynamic areas with strong currents and cold upwelling, and in the coastal zones. It is these areas that are of the most interest to SST users for various applications, including fishing, ship navigation, ocean dynamics analyses, marine biology studies, and recreation activities. Another large group of Level 2 SST users are producers of Level 4 SST analyses. Those too need more data in data sparse dynamic and coastal areas, to accurately reproduce SST gradients and fine structure of the SST fields.

4. Conclusion and future work

SST Pattern Test (SPT) supplemental to the current ACSPO clear-sky mask is being explored. Our preliminary analyses suggest that some limitations inherent to the current ACSM may be alleviated, and SST coverage improved. Globally, the SPT increases the ACSPO clear-sky domain by 0.2–0.3%. However, the improvements are highly non-uniform in space and time, and are mostly noticeable in the areas interesting to ACSPO users, including dynamic areas of the ocean and coastal zones, where the SPT may add up to 15% to the ACSPO clear-sky SST domain (cf. Fig. 16b). We plan to implement the current version of the SPT into ACSPO operations, comprehensively test its performance in globally and seasonally representative conditions, and fine-tune (with emphasis on minimizing the additional cloud leakages) and iteratively improve. Initially the SPT will be included in the ACSM as an additional restoral filter (i.e., it will only be applied to those pixels excluded from the SST domain by the ACSM, but identified as clear by the SPT). If the handling of false alarms in the ACSM by the current SPT proves successful, then the next step may be increasing the conservativeness of the ACSM (to minimize its cloud leakages) and processing a larger “cloudy” ACSM domain with the SPT. Ultimately, we plan to redesign the current ACSM based on pattern recognition principles, in conjunction with the heritage of current ACSM and broader cloud screening fundamentals. Work is also underway with the JPSS VIIRS Imagery Team (lead, Don Hillger) to explore the generation of a “Level 1.5” product in which destriping and resampling are applied. If created, such product would greatly facilitate the SPT process in ACSPO.

Acknowledgments

This work is conducted under the JPSS SST project funded by the JPSS Program Office, and the Ocean Remote Sensing Program funded by

NOAA. We thank Marouan Bouali, Karlis Mikelsons, John Stroup, Xingming Liang, Prasanjit Dash and John Sapper for the help with the data and useful discussions. We acknowledge Peter Hollemanns for the development of the CoastWatch Data Analysis Tool (available at http://coastwatch.noaa.gov/cwn/cw_software.html) used to generate some SST and clear-sky Figures. We also thank Drs. Don Hillger (NOAA) and Peter Minnett (U. Miami) for supporting our re-sampling efforts in the bow-tie areas, and anonymous reviewers for constructive feedback. The views, opinions, and findings contained in this paper are those of the authors and should not be construed as an official NOAA or US Government position, policy, or decision.

References

- Alliss, R.J., & Raman, S. (1995). Quantitative estimates of cloudiness over the Gulf Stream locale using GOES VAS observations. *Journal of Applied Meteorology*, 34, 500–510.
- Belkin, I.M., & O'Reilly, J.E. (2009). An algorithm for oceanic front detection in chlorophyll and SST satellite imagery. *Journal of Marine Systems*, 78, 319–326.
- Beucher, S. (1982). Watersheds of functions and picture segmentation. *Acoustics, speech, and signal processing, IEEE International Conference on ICASSP '82. IEEE*, Vol. 7. (pp. 1928–1931).
- Bouali, M., & Ignatov, A. (2014). Adaptive reduction of striping for improved sea surface temperature imagery from Suomi National Polar-orbiting Partnership (S-NPP) Visible Infrared Imaging Radiometer Suite (VIIRS). *Journal of Atmospheric and Oceanic Technology*, 31.
- Brasnett, B. (2008). The impact of satellite retrievals in a global sea-surface-temperature analysis. *Quarterly Journal of the Royal Meteorological Society*, 134, 1745–1760.
- Cao, C., Xiong, X.J., Wolfe, R., DeLucia, F., Liu, Q.M., Blonski, S., et al. (2013). *Visible infrared imaging radiometer suite (VIIRS) sensor data record (SDR) user's guide, version 1.2*. NOAA Technical Report NESDIS, 142A.
- Cayula, J.-F., & Cornillon, P. (1992). Edge detection algorithm for SST images. *Journal of Atmospheric and Oceanic Technology*, 9, 67–80.
- Cayula, J.-F., & Cornillon, P. (1995). Multi-image edge detection for SST images. *Journal of Atmospheric and Oceanic Technology*, 12, 821–829.
- Couprise, M., & Bertrand, G. (1997). Topological gray-scale watershed transformation. *Optical science, engineering and instrumentation '97* (pp. 136–146). International Society for Optics and Photonics.
- Farid, H., & Simoncelli, E.P. (2004). Differentiation of discrete multidimensional signals. *Image Processing, IEEE Transactions on*, 13, 496–508.
- Gonzalez, R.C., & Woods, R.E. (1992). *Digital image processing*. Addison-Wesley, 414–428.
- Haralick, R.M. (1983). Ridges and valleys on digital images. *Computer Vision, Graphics, and Image Processing*, 22, 28–38.
- Haralick, R.M. (1984). Digital step edges from zero crossing of second directional derivatives. *Pattern Analysis and Machine Intelligence, IEEE transactions on*, 58–68.
- Hillger, D., Kopp, T., Lee, T., Lindsey, D., Seaman, C., Miller, S., et al. (2013). First-light imagery from Suomi NPP VIIRS. *Bulletin of the American Meteorological Society*, 94, 1019–1029.
- Hillger, D., Seaman, C., Liang, C., Miller, S., Lindsey, D., & Kopp, T. (2014). Suomi NPP VIIRS imagery evaluation. *Journal of Geophysical Research, [Atmospheres]*, 119.
- Hutchison, K., Roskovensky, J., Jackson, J., Heidinger, A., Kopp, T., Pavoloski, M., et al. (2005). Automated cloud detection and classification of data collected by the visible infrared imager radiometer suite (VIIRS). *International Journal of Remote Sensing*, 26, 4681–4706.
- Jain, A.K., & Dubes, R.C. (1988). *Algorithms for clustering data*. Prentice-Hall, Inc.
- Jain, A.K., Murty, M.N., & Flynn, P.J. (1999). Data clustering: A review. *ACM Computing Surveys (CSUR)*, 31, 264–323.
- Meer, P., & Weiss, I. (1992). Smoothed differentiation filters for images. *Journal of Visual Communication and Image Representation*, 3, 58–72.
- Miller, P. (2009). Composite front maps for improved visibility of dynamic sea-surface features on cloudy SeaWiFS and AVHRR data. *Journal of Marine Systems*, 78, 327–336.
- Minobe, S., & Takebayashi, S. (2014). Diurnal precipitation and high cloud frequency variability over the Gulf Stream and over the Kuroshio. *Climate Dynamics*, 1–17.
- Petrenko, B., Ignatov, A., Kihai, Y., & Heidinger, A. (2010). Clear-sky mask for the advanced clear-sky processor for oceans. *Journal of Atmospheric and Oceanic Technology*, 27, 1609–1623.
- Roushdy, M. (2006). Comparative study of edge detection algorithms applying on the grayscale noisy image using morphological filter. *GVIP Journal*, 6, 17–23.
- Seaman, C., Hillger, D., Kopp, T., Williams, R., Miller, S., & Lindsey, D. (2014). *Visible Infrared Imaging Radiometer Suite (VIIRS) imagery environmental data record (EDR) user's guide, version 1.1*. Technical Report NOAA.
- Ullman, D.S., & Cornillon, P.C. (2000). Evaluation of front detection methods for satellite-derived SST data using in situ observations. *Journal of Atmospheric and Oceanic Technology*, 17.
- Vincent, L., & Soille, P. (1991). Watersheds in digital spaces: An efficient algorithm based on immersion simulations. *Pattern Analysis and Machine Intelligence, IEEE Transactions on*, 13, 583–598.